Ultrahigh-sensitivity liquid-core FMZI enabled by modal dispersion engineering with side-polished hollow-core interfaces

CHENG-LING LEE,[*] **Ⓓ YI-HUA WU, YING-ZHEN HUANG, AND BO-SHEN CHANG**

Department of Electro-Optical Engineering, National United University, Miaoli, 360, Taiwan
[*]*cherry@nuu.edu.tw*

Abstract: We present an ultrahigh-sensitivity liquid-core (LC) fiber Mach–Zehnder interferometer (FMZI) enabled by modal dispersion engineering and side-polished hollow-core interfaces. The proposed device integrates a 10 μm-core liquid-filled hollow-core fiber (HCF_{10}) between two side-polished large-core HCFs, forming an open microchannel that enables efficient filling with high thermo-optic coefficient (TOC) liquids. The modal dispersion of the liquid core is tailored such that the effective index difference between the core and cladding modes increases with wavelength (λ), resulting in a temperature-induced redshift in the interference spectrum. The optical interference behaviors of the dispersion-engineered structure reverse from those of conventional silica-core FMZIs. To the best of our knowledge, this is the first study to derive an explicit analytical formulation that quantitatively relates temperature sensitivity to the spectral dispersion of the effective index difference between the core and cladding modes under arbitrary refractive index dispersion conditions. Experimental results exhibit excellent agreement with theory, with average temperature sensitivities exceeding +80 nm/°C across multiple interference dips using Cargille liquid ($n_D = 1.46$) as the core medium. Our findings further demonstrate that temperature sensitivity strongly depends on the interference wavelength and the order of core–cladding mode coupling: shorter wavelengths and lower-order cladding modes produce higher sensitivities. The results of the agreement support the robustness of the proposed dispersion-engineered configuration for realizing predictable and adaptive temperature sensitivity in liquid-core fiber interferometers.

1. Introduction

Optical fiber Mach-Zehnder interferometer (FMZI) sensors have garnered significant attention recently due to their sensitivity, flexibility, and compact size, making them ideal candidates for various sensing applications. One of the primary reasons for their growing popularity is their remarkable advantages over traditional sensors. Unlike other types of fiber sensors, FMZI sensors enable multi-parameter sensing—such as temperature, strain, and refractive index—with high resolution and spectral stability. Their all-fiber transmission configuration allows convenient cascading or multiplexing along a single fiber link, facilitating distributed or multi-point sensing. They also support highly flexible structural configurations, including core–core, core–cladding, and core–hollow-core interference schemes, allowing precise tailoring of sensitivity for specific applications. Moreover, when compared with other interferometric schemes such as Fabry–Pérot or Sagnac interferometers, FMZIs offer relatively straightforward fabrication via standard splicing or side-polishing processes, without requiring reflective coatings, mirrors, or fused fiber couplers. These features make FMZI sensors highly versatile and suitable for application in various fields, including aerospace, biomedical engineering, environmental monitoring, and structural health assessment. Leveraging these advantages, researchers have developed and explored various Mach-Zehnder interferometric (MZI) sensor structures tailored for different sensing applications.

A wide range of fabrication techniques have been employed to create FMZI structures, including V-shaped cores (VCs) [1], core-offset splicing [2–5], tapered fibers [6–10], polished fibers [11–13], micro-bending cores [14], liquid-filled cores [15,16], optical fiber splicing techniques [17–20], and angled fiber cleaving [21]. These structures were designed to enhance the sensors' sensitivity to various parameters, such as temperature, refractive index (RI), and curvature. For instance, several FMZI configurations have been optimized for temperature and RI sensing [8,14,15], as well as for specific applications like concentration sensing [5,16], temperature sensing [2,3,6,7,11,12,20], RI sensing [1,4,9,13], curvature sensing [17,19], and such as combined curvature and temperature sensing [18]. The adaptability of FMZI sensors to different sensing requirements highlights their potential for widespread industrial and scientific applications.

The FMZI sensors are particularly effective in achieving high-accuracy measurements for tiny variations in environmental parameters such as temperature and displacement. Due to their high sensitivity and reliability, these optical fiber sensing devices have been applied in various fields, including structural health monitoring, chemical sensing, and biomedical diagnostics. Among the many FMZI sensor designs, liquid-filled structures have been especially promising for temperature measurement. Many studies have proposed liquid-filled FMZI designs that demonstrate enhanced temperature sensitivity. For example, an FMZI sensor that combines a spliced joint between a single-mode fiber (SMF) and a hollow-core fiber (HCF) infiltrated with isopropanol has achieved temperature sensitivities of -42.7 nm/°C [15]. While this design is simple to fabricate and cost-effective, its T-sensitivity is somewhat limited. To improve this, a core-offset spliced fiber sensor based on the FMZI principle, filled with refractive index-matching liquids, was developed and achieved a high T-sensitivity of 21.2 nm/°C [3]. Despite the enhanced sensitivity of this sensor, the low thermo-optic coefficient (TOC) of the material limited its T-sensitivity, preventing it from reaching optimal performance. Another design involves an FMZI sensor with a D-shaped fiber cavity filled with a liquid refractive index of 1.482, which exhibited ultrasensitivity to temperature, with a sensitivity of -33.72 nm/°C for RI of 1.456 [12]. However, the complex splicing process posed challenges for practical implementation. Additionally, a fused tilt-angle FMZI filled with various liquids of different refractive index, such as deionized water, ethanol, and Cargille liquids with refractive indices of 1.305 and 1.40, demonstrated temperature sensitivities of 0.8869, 4.4754, 4.8229, and 13.87 nm/°C, respectively [21]. These results indicate that liquids with higher TOCs lead to better T-sensitivity modulation. However, the above temperature sensitivities of several reported designs (with the exception of [12]) remain inadequate for high-precision and high-resolution applications requiring detection of temperature variations below 0.01 °C, such as biochemical reactions in microfluidic systems, ultra-stable photonic devices, or thermally tunable optical filters with stringent stability requirements.

Although prior studies have focused on manipulating either the core or cladding materials to tailor the sensing response of FMZI structures, few have investigated the control of modal dispersion via the refractive index dispersion characteristics of the materials themselves. Therefore, this study, we propose and experimentally demonstrate a novel dispersion-engineered liquid-core fiber Mach–Zehnder interferometer (LCFMZI) that achieves ultrahigh temperature sensitivity by combining tailored modal dispersion with thermally induced refractive index modulation. The device integrates a 10 μm-core hollow-core fiber (HCF_{10}) with dual side-polished large-core HCF, forming an open microchannel that allows efficient filling with high-TOC, dispersion-engineered liquids. This configuration enables a temperature-induced redshift in the interference spectrum using Cargille liquids (n_D = 1.46), demonstrating exceptional T-sensitivities exceeding 80 nm/°C, (and in some cases greater than 100 nm/°C). To the best of our knowledge, this is the first work to derive an explicit analytical formulation that quantitatively relates the temperature sensitivity of LCFMZI sensors to the spectral dispersion of the effective index difference between the core and cladding modes, under arbitrary refractive index dispersion conditions of the filled medium. This

breakthrough lays a theoretical foundation for optimizing next-generation FMZI sensors across a variety of waveguide designs.

2. Theoretical analysis of dispersion-engineered LCFMZI

The configuration and interference principle of the proposed LCFMZI is illustrated in Fig. 1.
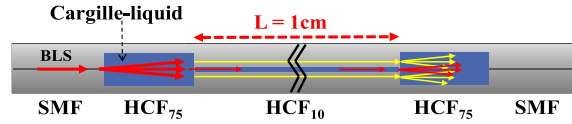
Fig. 1. Schematic diagram of configuration and interference principle of the proposed LCFMZI.

Here, HCF_{75} and HCF_{10} denote to the core diameters of the hollow-core fibers, measuring 75 µm and 10 µm, respectively. The broadband optical light source (BLS), with a wavelength range of 1250–1650 nm, is launched into the input SMF and propagates into the first HCF_{75} segment, where the optical field expands before entering the HCF_{10} - serving as the main interference region. Within the first HCF_{75} region, the light splits primarily into two paths: the cladding and the core. Unlike obliquely incident light, which would excite higher-order core modes (e.g., LP_{11}) [22], the weakly guided single-core mode configuration here supports only the fundamental LP_{01} mode. However, multiple cladding modes can be simultaneously excited in the waveguide structure. Due to the effective optical path difference (OPD) between the core mode and cladding modes, multimode interference is generated. The optical fields from all excited modes recombine in the second HCF_{75} segment, creating constructive and destructive interference patterns in the output SMF. These interference spectra are subsequently measured and analyzed.

To enhance the understanding of the proposed dispersion-engineered waveguide characteristics, we conducted a theoretical analysis and compared it with a standard single-mode fiber 28 (Corning SMF-28). First, we derived the relationship between the effective index of the guided modes and the interference wavelength shifts during optical transmission in the FMZI waveguide. The effective indices of the core and cladding modes were calculated using fiber waveguide theory. Figure 2(a) illustrates the material dispersion curves of the refractive indices (RIs) for the optical fibers and liquid used in the setup. The RIs of the silica core, and silica cladding, corresponding to a wavelength (λ) range of 1250~1650 nm, are denoted as n_{silica_core}, and n_{clad}, respectively. The Sellmeier equation is used to describe the RI as: $n^2 = \left(\frac{a_1\lambda^2}{\lambda^2-b_1}\right) + \left(\frac{a_2\lambda^2}{\lambda^2-b_2}\right) + \left(\frac{a_3\lambda^2}{\lambda^2-b_3}\right) + 1$ (λ is in µm) The coefficients a_1, a_2, a_3, b_1, b_2 and b_3 are Sellmeier coefficients [22]. The cladding RI, n_{clad} is calculated with the parameters $a_1 = 0.6961663$, $a_2 = 0.4079426$, $a_3 = 0.8974994$, $b_1 = 0.004679148$, $b_2 = 0.01351206$ and $b_3 = 97.934002$. Similarly, the silica core RI for a general SMF-28 is determined using $a_1 = 0.700071$, $a_2 = 0.421598$, $a_3 = 0.888017$, $b_1 = 0.004596176$, $b_2 = 0.01448869$ and $b_3 = 98.203859$ [23]. For the liquid core (n_{core}) using the Cargille liquid with $n_D = 1.46$ and its RI in the proposed configuration is determined using the Cauchy equation: $n = A + \frac{B}{\lambda^2} + \frac{C}{\lambda^4}$, where $A = 1.447925$, $B = 4.0734 \times 10^3$, $C = 4.1636939 \times 10^7$ with the wavelength λ in nm [24].

The dispersion equations for the linearly polarized (LP) modes describe the approximate solutions for weakly guided fiber, where the longitudinal electric and magnetic field components (E_z and H_z) are nearly zero, making the modes primarily transverse. For the $LP_{m\ell}$ mode with single mode $m = 0$ and $\ell = 1$, the characteristic equation governing optical waveguides, particularly for cylindrical waveguides, is given as [25]:

$$\frac{J_0(u)}{uJ_1(u)} = \frac{K_0(w)}{wK_1(w)} \tag{1}$$
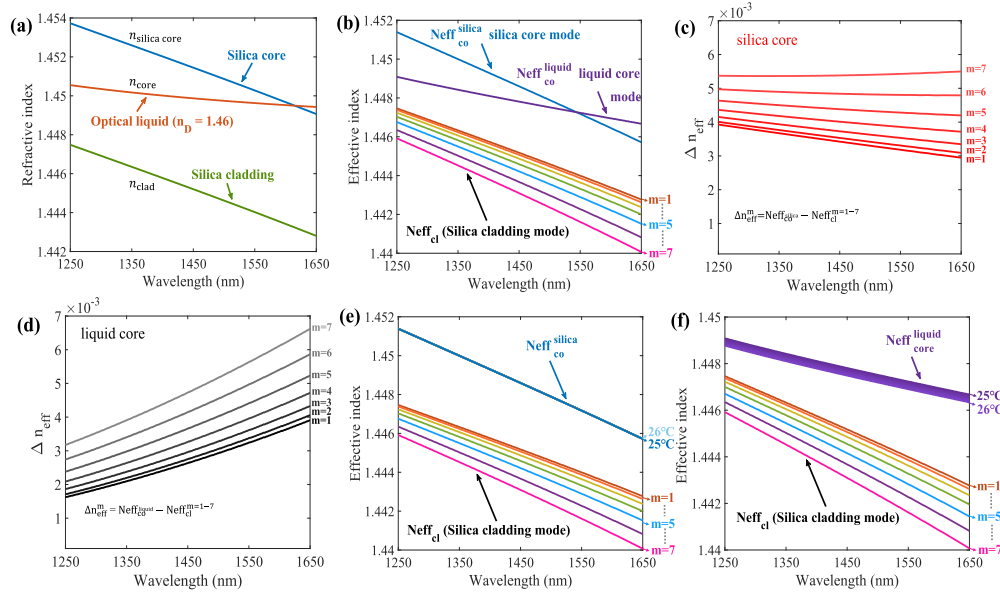
Fig. 2. (a) RI dispersion curves for silica core, silica cladding, and liquid core. (b) Effective indices of the fundamental silica and liquid core modes, and the first seven cladding modes. (c) Wavelength dependence of Δn_{eff}^m for the silica core waveguide. (d) Corresponding results for the liquid core, showing an inverse trend of Δn_{eff} compared to (c). (e) Temperature-dependent variations in the silica-core effective index. (f) Temperature-dependent variations in the liquid-core effective index, greater sensitivity due to its high TOC.

Here, $J_0(u)$ and $J_1(u)$ are Bessel functions of the first kind, which describe the behavior of electromagnetic fields inside the waveguide core. $K_0(u)$ and $K_1(u)$ are modified Bessel functions of the second kind representing the decaying field in the cladding region. u and *w* are parameters that define the radial field distribution as $u = a\sqrt{k^2 n_{\text{core}}^2 - \beta^2}$ represents the transverse wave propagation in the core and is associated with the Bessel function $J(u)$, while $w = a\sqrt{\beta^2 - k^2 n_{\text{clad}}^2}$ represents the transverse decay in the cladding and is associated with the modified Bessel function $K(w)$. In these expressions, $k = \frac{2\pi}{\lambda}$ is the free-space wavenumber and λ is the wavelength of light. β is the propagation constant and *a* is the core radius of a hollow-core fiber (HCF) with a diameter of 10μm. The actual diameter of the HCF has a manufacturing tolerance of about ± 2μm [26]. From Eq. (1), the propagation constant: β can be determined by solving the characteristic equation for the given waveguide structure and material dispersion curves of the RI shown in Fig. 2 (a). In Fig. 2(a), we can see that the silica core and cladding of SMF-28 are more dispersive to the wavelength (λ) than those of the filled Cargille-liquid of $n_D = 1.46$. The RI profile (red line) of the liquid core shows much flat material dispersion with wavelength.

Thus, once β is obtained, the effective index (n_{eff}) of the mode can be calculated using the following relation: $n_{\text{eff}} = \beta/k$. Figure 2(b) shows the effective index of the fundamental silica core mode ($\text{Neff}_{\text{co}}^{\text{silica}}$) of a Corning SMF-28 fiber, LP$_{01}$ fundamental liquid core mode ($\text{Neff}_{\text{co}}^{\text{liquid}}$.), and the first seven order cladding modes ($\text{Neff}_{\text{cl}}^{m=1-7}$) [27]. To further study the sensitivity of the proposed LCFMZI, the T characteristics of the materials need to be analyzed. The temperature derivative of the refractive index of the Cargille-liquid with $n_D = 1.46$ in the liquid core with $-3.89 \times 10^{-4}\ °C^{-1}$ [24] has a negative characteristic which is almost two orders of magnitude higher than that of the silica core fiber. The difference in effective index is defined

as $\Delta n_{\text{eff}}^m = \text{Neff}_{\text{co}}^{\text{silica}} - \text{Neff}_{\text{cl}}^{m=1-7}$, between the fundamental silica core mode and the mth-order cladding modes (m = 1-7) at 25°C is calculated and presented in Fig. 2(c).

Subsequently, $\Delta n_{\text{eff}}^m = \text{Neff}_{\text{co}}^{\text{liquid}} - \text{Neff}_{\text{cl}}^{m=1-7}$, the difference of effective index between the LP_{01} liquid core and the mth-orde(m = 1-7) cladding modes at 25°C are determined and they are shown in Fig. 2(d). The results in Fig. 2(c) and Fig. 2(d) illustrate the contrasting behavior of the Δn_{eff}^m for the silica-core and liquid-core waveguides, respectively. In Fig. 2(c), which corresponds to the silica-core case, the curves exhibit a monotonic decrease with increasing wavelength, indicating that the Δn_{eff}^m decreases as the wavelength increases.

Conversely, in Fig. 2(d), representing the liquid-core case, the curves show an inversely increasing curve, where Δn_{eff}^m increases with wavelength. This opposite behavior is attributed to the unique dispersion properties of the liquid-core medium, where the refractive index contrast between the core and cladding grows with increasing wavelength, leading to enhanced mode confinement. When the T changes from 25°C to 26°C, the RI of the silica core mode ($n_{\text{silica\_core}}$) changes, but it only has a minimal effect on the effective index of the silica core ($\text{Neff}_{\text{co}}^{\text{silica}}$) due to its small TOC, as shown in Fig. 2(e). However, in Fig. 2(f), the RI of the liquid core mode (n_{core}) changes, leading to a corresponding reduction in the $\text{Neff}_{\text{co}}^{\text{liquid}}$ with significant variations. In the condition, the cladding modes remain almost unchanged when the T varies since the TOC of the fused silica $+ 8.6 \times 10^{-6}$ °C^{-1} is relatively small. After formulating the theoretical model and determining the modes of the proposed optical fiber waveguide structure with the specific liquid core, the next step is to analyze its interference characteristics. The following Eq. (2) describes the interference mechanism. I_{co} and I_{cl}^m indicate the light intensity of the liquid core and the mth-order cladding modes, respectively. Here, the parameter I can be regarded as the transmission output of the interference.

$$I = I_{\text{co}} + I_{\text{cl}}^m + 2\sqrt{I_{\text{co}} I_{\text{cl}}^m} \cos(\phi_m) \qquad (2)$$

Here, the phase difference (ϕ_m) between the core and m^{th}-order cladding modes can be deduced as Eq. (3) with the transmission path of interference L of HCF_{10}.

$$\phi_m = \frac{2\pi}{\lambda}(\text{Neff}_{\text{co}} - \text{Neff}_{\text{cl}}^m)L = \frac{2\pi}{\lambda}\Delta n_{\text{eff}}^m L \qquad (3)$$

Here, Neff_{co} is the effective index of the liquid core mode, λ represents the wavelength of light in a vacuum, and Δn_{eff}^m denotes the difference in the effective index between the liquid core mode and the mth-order cladding modes. As this difference in effective index changes, it also influences the wavelengths that must meet the same phase difference condition. In other words, during constructive or destructive interference, the locations of the interference wavelengths in the spectra adjust, leading to shifts in the interference peaks and dips. As a result, the wavelength corresponding to the interference dip in the spectra (λ_{dip}^m) can be determined from the condition of destructive interference (i.e., $\phi_m = (2p + 1)\pi$). In the following section, by deriving Eq. (4), the Δn_{eff}^m, with p being a positive integer representing the interference orders in the optical spectra.

$$\Delta n_{\text{eff}}^m = \frac{(2p + 1) \times \lambda_{\text{dip}}^m}{2L} \qquad (4)$$

Based on the Δn_{eff}^m corresponding to m = 1-7 in Fig. 2(d), we further evaluate the interference orders p over wavelengths ranging from 1250 nm to 1650 nm, using the actual interference length L = 1 cm by Eq. (4). The calculation results, shown as colored lines in Fig. 3, illustrate the distribution of different p values across the measured wavelength range. The intersections of these curves correspond to the interference wavelength dip locations for their respective m^{th}-order cladding mode interferences. However, when the LP_{01} core mode couples with multiple
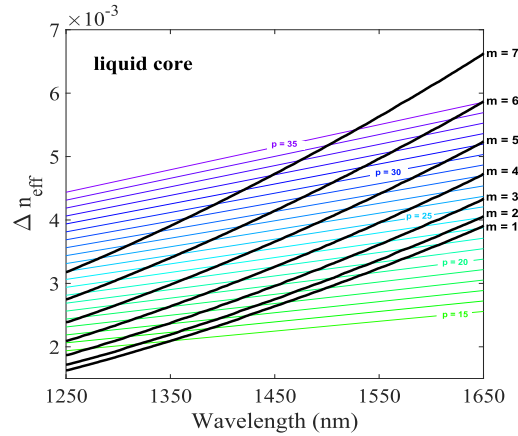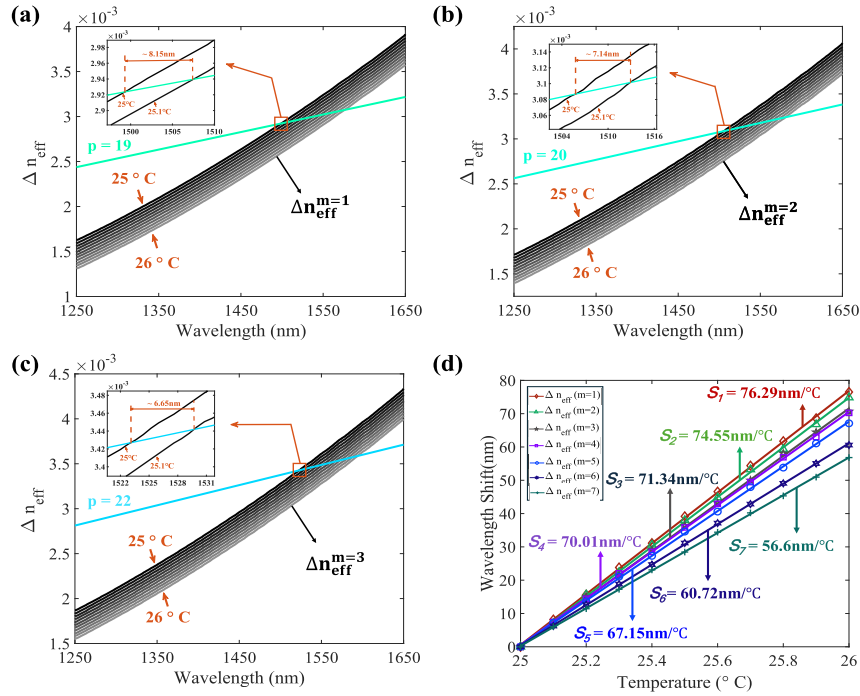
Fig. 3. Difference of effective refractive index ($\Delta n_{\text{eff}}^{m}$) between the core mode and m = 1 to 7 cladding modes over the interference order of p = 15 to 35.

m^{th}-order cladding modes, it leads to a complex superposition of modes, resulting in a composite interference pattern.

To investigate the unique dispersion properties of the proposed LCFMZI, we analyze the interference behavior for each mth cladding mode under a temperature variation from 25 °C to 26 °C with 0.1 °C increments. The corresponding results are presented as black line groups in Fig. 4(a)–(c), where each line represents the first- to third-order cladding modes. We assessed the theoretical sensitivity by identifying the intersection points of selected p-values with different m-order cladding mode interference curves within the 1450–1550 nm spectral band, as shown in Fig. 4(a)–(c) with p = 19, 20, and 22 corresponding to m = 1, 2, and 3. As illustrated in the insets of Fig. 4(a)–(c), a temperature increase of +0.1 °C (from 25.0 °C to 25.1 °C) leads to notable redshifts of approximately 8.15 nm, 7.14 nm, and 6.65 nm, indicating a strong thermal response across multiple interference orders. The total wavelength shifts over the whole temperature range (25 °C to 26 °C) were also calculated, yielding T sensitivities of approximately 76.29 nm/°C, 74.55 nm/°C, and 71.34 nm/°C. We further applied the same calculation method used in Fig. 4(a)–(c) to evaluate the m = 4 to 7 cladding modes, obtaining corresponding sensitivities of 70.01 nm/°C, 67.15 nm/°C, 60.72 nm/°C, and 56.60 nm/°C, as shown in Fig. 4(d). These results demonstrate that higher cladding mode orders (larger m) reduce thermal sensitivity. Moreover, regardless of the interference order, the dip wavelength λ_{dip}^{m} remains highly responsive to temperature changes, highlighting the exceptional thermal sensitivity of the proposed fiber structure, which is enabled by its tailored dispersion engineering.

Building upon the theoretical analysis presented in Fig. 4, we further employ Eq. (1) to derive the temperature dependence of the effective refractive index (n_{eff}) of the waveguide liquid core mode (Neff$_{\text{co}}$). The derivation begins with the characteristic equation involving Bessel functions, which relates to the radial field distribution of the core and cladding regions Eq. (1). The equation is expressed in terms of two variables, u and ω, which are functions of the refractive indices of the core, cladding, and effective core mode. By differentiating these variables with respect to temperature (T), we obtain expressions for du/dT and $d\omega/dT$, which incorporate the thermal-optic coefficients (dn/dT) of the core and cladding materials, as Eq. (5). The temperature derivative of the characteristic equation is then evaluated by applying the chain rule to both sides, yielding a relationship between the partial derivatives of the Bessel function ratios and the temperature-dependent shifts of u and ω. These partial derivatives are denoted as weighting

Fig. 4. (a)–(c) show the temperature dependence of the effective refractive index difference (Δn_{eff}^{m}) between the core mode and the first three cladding modes (m = 1 to 3), along with their corresponding interference orders *p*. The intersection points indicate temperature-dependent behavior from 25 °C to 26 °C. (d) Corresponding temperature sensitivities were extracted by linear fitting the intersection points for cladding modes m = 1–7.

factors (F_1 and F_2), as Eq. (6), which quantifies the respective contributions of the core and cladding refractive index variations to the overall thermal sensitivity of the effective index.

Finally, by solving the resulting equation, we derive a closed-form expression for $dNeff_{co}/dT$, as shown in Eq. (7). This formulation clearly reveals how the thermal responses of the core and cladding refractive indices in association influence the waveguide's effective index of the liquid core mode, providing valuable understanding into the thermal behavior of the proposed structure.

$$\left[\frac{\partial}{\partial u} \left(\frac{J_0(u)}{u J_1(u)} \right) \right] \frac{du}{dT} = \left[\frac{\partial}{\partial \omega} \left(\frac{K_0(\omega)}{\omega K_1(\omega)} \right) \right] \frac{d\omega}{dT} \tag{5}$$

$$F_1 = \frac{\partial}{\partial u} \left(\frac{J_0(u)}{u J_1(u)} \right) , \ F_2 = \frac{\partial}{\partial \omega} \left(\frac{K_0(\omega)}{\omega K_1(\omega)} \right) \tag{6}$$

$$\frac{dNeff_{co}}{dT} = \frac{n_{core} \frac{dn_{core}}{dT} F_1 - n_{clad} \frac{dn_{clad}}{dT} F_2}{Neff_{co}(F_1 + F_2)} \tag{7}$$

After determining the temperature dependence of the effective refractive index of the liquid core mode ($Neff_{co}/dT$), we proceed to apply the Eq. (7) to analyze the relationship between the resonance wavelength dip (λ_{dip}^{m}) and the temperature variation. By differentiating Eq. (4) with respect to temperature, the resulting expression is presented as Eq. (8). To the best of our knowledge, Eq. (8), $\frac{d\lambda_{dip}^{m}}{dT} \equiv S_m$ represents temperature sensitivity, which is the first analytical formulation in the literature that explicitly evaluates the thermal performance of fiber Mach-Zehnder interferometer (FMZI)-based optical fiber waveguide structures incorporating arbitrary

refractive index dispersion profiles.

$$\frac{d\lambda_{dip}^m}{dT} = \frac{-\frac{\partial(\Delta n_{\text{eff}}^m)}{\partial T}}{\frac{\partial(\Delta n_{\text{eff}}^m)}{\partial \lambda} - \frac{(2p+1)}{2L}} = \frac{-\left(\frac{\partial \text{Neff}_{\text{co}}}{\partial T} - \frac{\partial \text{Neff}_{\text{cl}}^m}{\partial T}\right)}{\frac{\partial(\Delta n_{\text{eff}}^m)}{\partial \lambda} - \frac{(2p+1)}{2L}} \tag{8}$$

To further analyze Eq. (8), the terms $\frac{\partial \text{Neff}_{\text{co}}}{\partial T}$ and $\frac{\partial \text{Neff}_{\text{cl}}^m}{\partial T}$ represent the temperature dependence of the effective refractive indices of the liquid core and silica cladding modes, which are associated with their TOCs. In this studied waveguide structure, $\frac{\partial \text{Neff}_{\text{co}}}{\partial T}$ is a significant negative value of the liquid core, whereas $\frac{\partial \text{Neff}_{\text{cl}}^m}{\partial T}$ of the silica cladding is a relatively small positive value. As a result, the numerator in Eq. (8) remains positive. Moreover, the denominator contains the term $\frac{\partial(\Delta n_{\text{eff}}^m)}{\partial \lambda}$, which characterizes whether the resonance wavelength shift in the FMZI exhibits a redshift or blueshift in response to the temperature. The parameter $\frac{\partial(\Delta n_{\text{eff}}^m)}{\partial \lambda}$ represents the wavelength-dependent variation of the effective refractive index difference between the core and the cladding mode of order *m*. In this study, the filling liquid with dispersion characteristic can achieve the $\frac{\partial(\Delta n_{\text{eff}}^m)}{\partial \lambda}$ positive and redshift. As demonstrated in Fig. 2(d) above, our proposed fiber interferometric configuration yields a positive $\frac{\partial(\Delta n_{\text{eff}}^m)}{\partial \lambda}$, while the term $\frac{(2p+1)}{2L}$ is a small constant (e.g., L = 1 cm = 10^7 nm), resulting in a positive denominator overall. Here, the denominator term $\frac{\partial(\Delta n_{\text{eff}}^m)}{\partial \lambda}$ represents the rate of change of the effective refractive index difference (Δn_{eff}^m) with respect to wavelength (λ), which is influenced by the dispersive properties of the material refractive index. Taken together, when both the numerator and denominator are positive, $\frac{d\lambda_{dip}^m}{dT}$ is also positive, indicating a redshift of the interference spectrum, which agrees with the trends shown in Fig. 4. Conversely, if $\frac{\partial(\Delta n_{\text{eff}}^m)}{\partial \lambda}$ becomes negative due to material design, then $\frac{d\lambda_{dip}^m}{dT}$ would be negative, corresponding to a blueshift. Therefore, this work, for the first time, proposes that by tailoring the dispersion characteristics $\frac{\partial(\Delta n_{\text{eff}}^m)}{\partial \lambda}$ and the thermo-optic coefficient $\frac{\partial \text{Neff}_{\text{co}}}{\partial T}$ of the used materials, the thermal response of the FMZI-based interference spectra can be flexibly and precisely engineered. These findings also demonstrate that in the proposed LCFMZI, the T-sensitivity characteristic exhibits a redshift in wavelength as T increases. Compared to the previously mentioned optical fiber sensors [12,15], this structure exhibits a distinct thermal response characteristic, further confirming its potential for sensing applications. In the following analysis, we determine the *m*-order T-sensitivity (S_m) using the parameter $\frac{d\lambda_{dip}^m}{dT}$, quantifying the resonance wavelength shift induced by temperature variation. By substituting the values into Eq. (8) with cladding mode orders *m* = 1–7 and their corresponding interference orders *p* = 19, 20, 22, 23, 25, 30 and 34 the T-sensitivity values λ_{dip}^m for interference dips located around 1500 nm are obtained. The results are presented in Fig. 5(a), showing that $S_1 = 81.75$ nm/∘C, $S_2 = 80.43$ nm/∘C, $S_3 = 78.53$ nm/∘C, $S_4 = 72.81$ nm/∘C, $S_5 = 67.40$ nm/∘C, $S_6 = 64.76$ nm/∘C, and $S_7 = 59.69$ nm/∘C for m = 1-7, which closely match the results in Fig. 4. Furthermore, we investigated the relationship between T-sensitivity and wavelength. Figure 5(b) presents theoretical results for p = 20, with dips located at approximately 1300 nm and 1500 nm. At $\lambda \approx 1300$ nm, the T-sensitivities are significantly higher: $S_1 = 121.90$ nm/∘C, $S_2 = 115.72$ nm/∘C, $S_3 = 106.04$ nm/∘C, $S_4 = 94.60$ nm/∘C, $S_5 = 82.90$ nm/∘C, $S_6 = 71.91$ nm/∘C, $S_7 = 62.10$ nm/∘C. In contrast, when the dips are located near 1500 nm, the values decrease to $S_1 = 83.80$ nm/∘C, $S_2 = 80.43$ nm/∘C, $S_3 = 75.00$ nm/∘C, $S_4 = 68.34$ nm/∘C, $S_5 = 61.22$ nm/∘C, $S_6 = 54.24$ nm/∘C, $S_7 = 47.75$ nm/∘C. Figure 5(c) extracts the sensitivities (S_m) from Fig. 5(a) at $\lambda_{dip}^m \approx 1500$ nm and plots them directly against cladding-mode order of *m* = 1–7, enabling a one-glance valuation of how m influences S_m for the same wavelength. Figure 5(d) repeats the analysis for Fig. 5(b) but separates the two wavelengths ($\lambda_{dip}^m \approx 1300$ nm and 1500 nm), highlighting the difference in the wavelength variation of S_m as m increases. The results indicate lower cladding mode orders, *m*

and shorter resonance wavelengths lead to higher T-sensitivity, whereas higher m values and longer wavelengths result in lower T-sensitivity in the proposed fiber waveguide structure. The results demonstrate that shorter wavelengths yield significantly higher T-sensitivities across all m values.
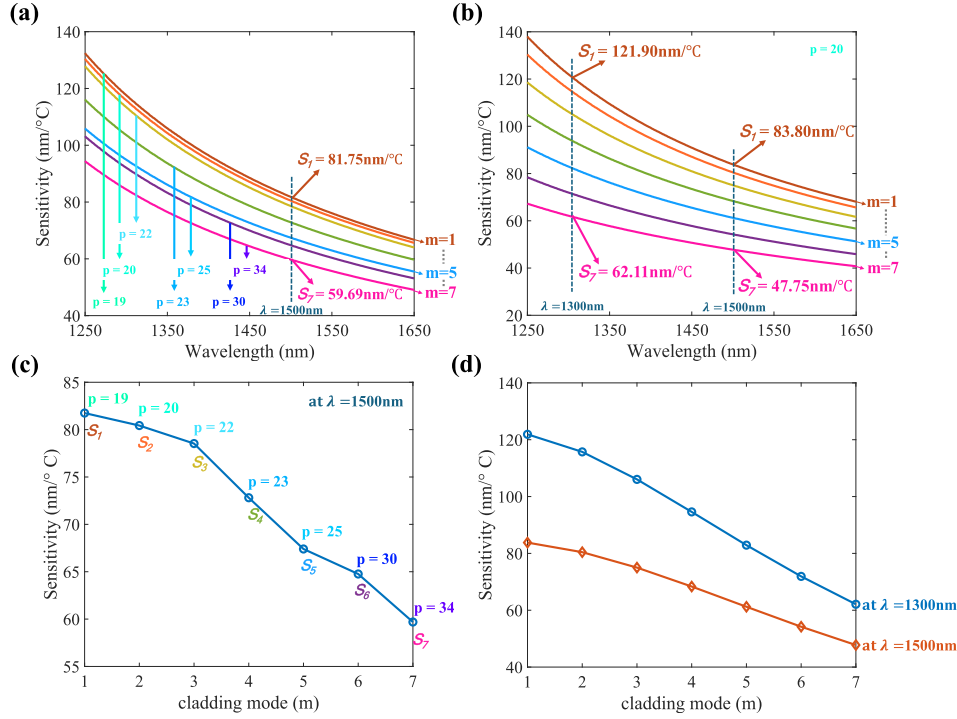

Fig. 5. T-sensitivity $\frac{d\lambda_{dip}^m}{dT}$ vs. wavelength, determined by Eq. (8), for cladding modes $m = 1$–7. (a) T-sensitivity trends for different m with $\lambda_{dip}^m \approx 1500$ nm, using their corresponding interference orders p (b) Comparison of T-sensitivity at two wavelengths $\lambda_{dip}^m \approx 1300$ nm and $\lambda_{dip}^m \approx 1500$ nm for fixed interference order $p = 20$. (c) The sensitivities at $\lambda_{dip}^m \approx 1500$ nm for m = 1–7 based on (a). (d) The sensitivities at $\lambda_{dip}^m \approx 1500$ nm for m = 1–7 based on (b) with the same interference order (p = 20).

3. Fabrication, experimental results, and discussion

To validate the theoretical analysis, a series of experiments were conducted to investigate the interference characteristics and temperature sensitivity of the proposed dispersion-engineered LCFMZI. The fabrication procedure, illustrated in Fig. 6(a), consists of four key steps. Step 1: A standard single-mode fiber (SMF) was spliced to a large hollow-core fiber (HCF$_{75}$, core diameter: 75 μm), which was subsequently polished to remove the cladding and exposed a tiny hole.

Step 2: The cleaved end of the HCF$_{75}$ was flattened to retain a micro-scale open region, then fused to a flat-cleaved SMF, forming a polished HCF$_{75}$ segment with a typical length of L$_s$ ≈ 300 μm. Step 3: A short segment of small-diameter hollow-core fiber (HCF$_{10}$, core diameter: 10 μm, length L = 1 cm) was inserted between two polished HCF$_{75}$ segments and fusion-spliced to establish the liquid-core region. Step 4: Steps 1 and 2 were repeated on the opposite end of the HCF$_{10}$ to complete the microchannel structure. The sensor was then filled with Cargille liquid (refractive index n$_D$ = 1.46). To avoid air bubble formation and ensure reliable liquid infiltration

into the main liquid-core region (HCF$_{10}$, L = 1 cm), we suspended the sensor horizontally with both ends exposed. The liquid was filled from only one side, while the opposite port is left open to allow pressure equalization and continuous capillary flow. As a result, capillary-driven filling proceeded smoothly, with no visible air bubble formation observed under microscope examination. Microscope images of the fabricated LCFMZI structure before and after liquid filling are shown in Figs. 6(b) and 6(c), respectively. As previously reported [15], performing fiber fusion after liquid injection may cause liquid evaporation due to high-temperature arc discharge, often resulting in fabrication failure. To address this issue, we adopt a pre-fusion approach that uses ultra-short, pre-polished HCF$_{75}$ segments at both ends of the HCF$_{10}$ section before filling. This design creates a micro-scale open channel that facilitates stable and efficient post-filling with various liquids [28], thereby greatly improving the flexibility and success rate of LCFMZI sensor fabrication.
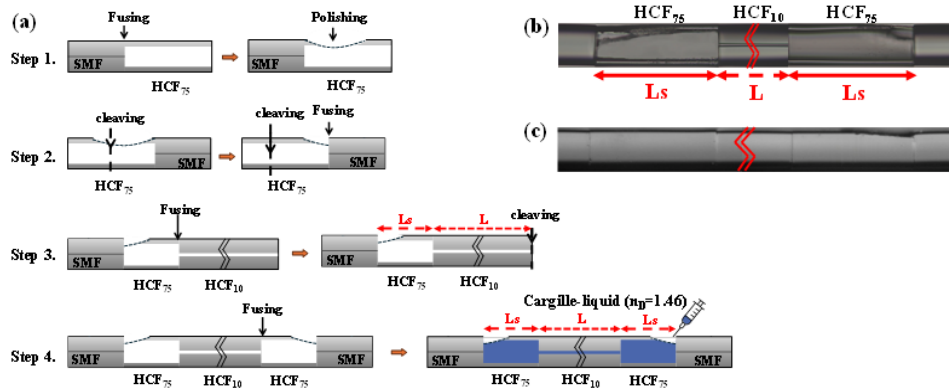

Fig. 6. (a) Schematic of the LCFMZI fabrication process comprising four steps to form a microchannel structure suitable for post-filling. (b) Microscope image of the sensor before liquid injection: the inserted HCF$_{10}$ has a length of 1 cm, and the polished HCF$_{75}$ segments at both ends have lengths $L_s \approx 300$ μm. (c) Microscope image of the completed structure after filling with Cargille liquid ($n_D = 1.46$).

Our experimental setup consists of a broadband light source (BLS) SLED module, which generates an interference spectrum through the LCFMZI. The temperature (T) is precisely controlled using a TE-cooler with a resolution of 0.05 °C to induce a thermal effect. The resulting spectral response is recorded using an optical spectrum analyzer (OSA) (Advantest Q8381A) with a resolution setting of 0.4 nm due to its high sensitivity. Figure 7(a) shows the initial optical interference spectrum of the fabricated LCFMZI device with L = 1 cm and $L_s \approx 300$ μm. To further analyze the spectral characteristics, the transmission spectrum is converted into a linear scale, as shown in Fig. 7(b), and subsequently processed using the Fast Fourier Transform (FFT) method, as plotted in Fig. 7(c). The FFT spectrum reveals multiple interference contributions and their associated spatial frequencies. A dominant primary peak appears at a spatial frequency of $fs_1 = 0.015$ nm^{-1}, corresponding to a free spectral range (FSR) of approximately 66.66 nm.

The dominant frequency indicates the strongest interference contribution and is considered for further analysis. The FSR of the LCFMZI is defined as the wavelength spacing between adjacent interference dips or peaks and is given by:

$$\text{FSR} = \frac{\lambda_1 \lambda_2}{(\text{Neff}_{co} - \text{Neff}_{cl}^m)L} \qquad (9)$$

Here, λ_1 and λ_2 ($=\lambda_1 + \text{FSR}$) represent the wavelengths of neighboring peaks or dips in the interference spectrum. L denotes the length of the HCF$_{10}$, while Neff$_{co}$ and Neff$_{cl}^m$ correspond to
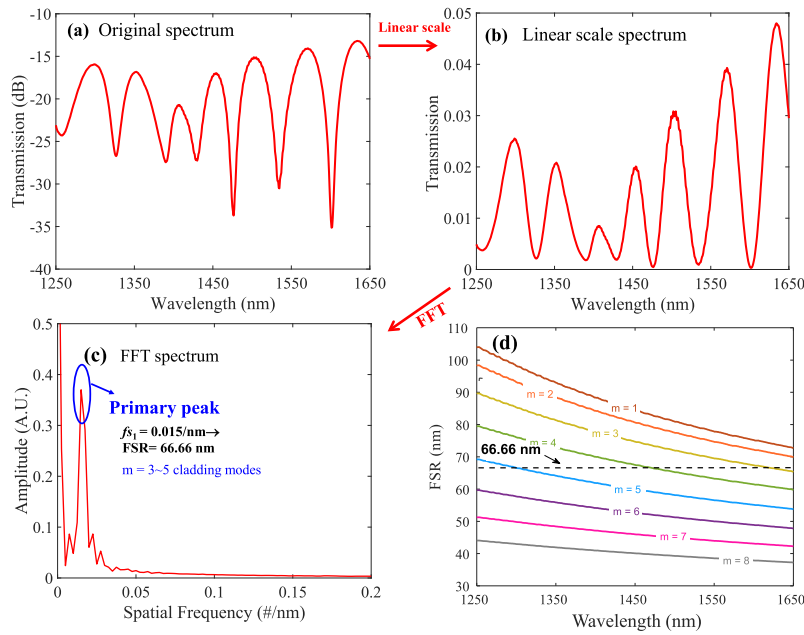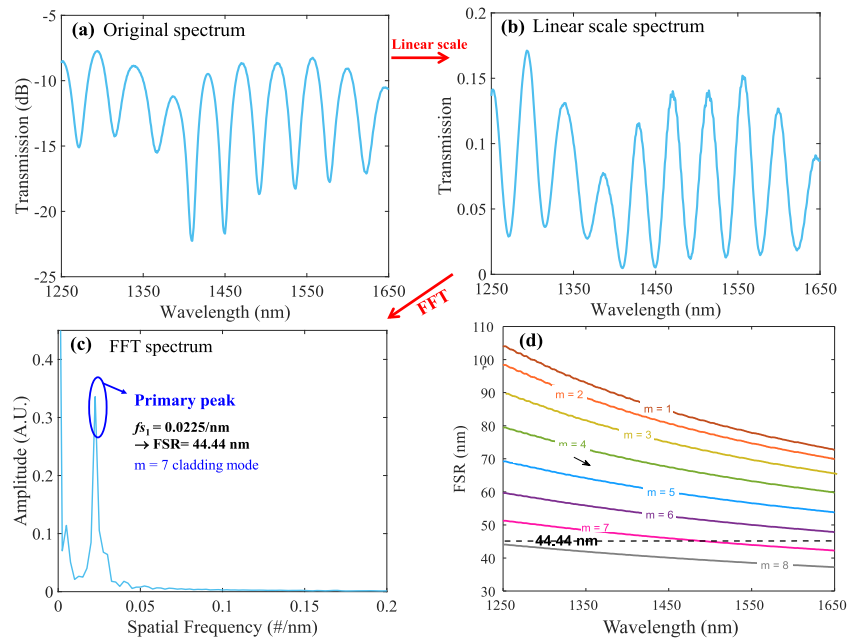
Fig. 7. (a) Transmission spectrum of the fabricated LCFMZI (L = 1 cm, $L_s \approx 300$ μm). (b) Spectrum converted to linear scale for FFT analysis. (c) FFT spectrum showing a dominant peak at spatial frequency $fs_1 = 0.015$ nm^{-1}, corresponding to FSR = 66.66 nm, primarily attributed to interference between the core mode and cladding modes m = 3–5. (d) Calculated FSR vs. wavelength for cladding modes m = 1–8, indicating that m = 3–5 best matches experimental results.

the effective refractive indices of the liquid core and the mth order cladding modes in the LCFMZI, respectively. The calculated FSR values vs. wavelength corresponding to core–cladding mode interference for m = 1–8 by Eq. (9) are shown in Fig. 7(d). Notably, the experimentally observed FSR of 66.66 nm aligns most closely with the theoretical curves of m = 3–5, indicating that these mid-order cladding modes contribute most significantly to the interference effect. These results confirm that cladding modes with m = 3–5 dominate the interference pattern in the fabricated LCFMZI, shaping the transmission spectrum across the wavelength range of 1250–1650 nm.

To further investigate the effect of the microchannel length (L_s) on the interference, an additional LCFMZI device was fabricated under identical conditions, except with a longer HCF$_{75}$ section yielding $L_s \approx 400$ μm. The resulting transmission spectrum and its corresponding FFT analysis are presented in Fig. 8(a–c). A distinct primary peak is observed at a spatial frequency of $fs_1 = 0.0225$ nm^{-1}, corresponding to a free spectral range (FSR) of 44.44 nm. Compared to the previous result in Fig. 7, this smaller FSR indicates a change in dominant cladding mode contribution. According to the theoretical curves shown in Fig. 8(d), the experimental FSR matches most closely with the m = 7 order cladding mode.

The result suggests that increasing L_s effectively would modify the interference condition, thereby enabling mode-selective transmission of specific cladding modes in the output spectrum.

To experimentally validate the theoretical predictions regarding temperature sensitivity presented in earlier sections, we performed thermal measurements on fabricated LCFMZI devices with two different side-polished segment lengths ($L_s \approx 300$ μm and 400 μm). As illustrated in Figs. 9 and 10, we tracked the wavelength shifts of selected interference dips (dip1 and dip2) over a controlled temperature range of 25.0 °C to 26.0 °C, with 0.1 °C increments. The selected dips

Fig. 8. (a) Transmission spectrum of the fabricated LCFMZI (L = 1 cm, $L_s \approx 400$ μm). (b) Spectrum converted to a linear scale for FFT analysis. (c) FFT spectrum showing a dominant peak at spatial frequency $fs_1 = 0.0225$ nm^{-1}, corresponding to FSR = 44.44 nm, primarily attributed to interference between the core mode and cladding modes m = 3–5. (d) Calculated FSR vs. wavelength for cladding modes m = 1–8, indicating that only m = 7 best matches experimental results.
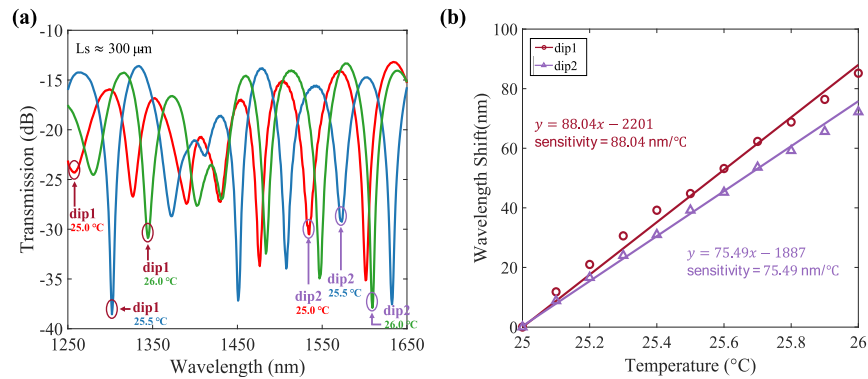
Fig. 9. (a) Evolution of the interference spectra as the temperature increases from 25.0 °C to 26.0 °C, showing the wavelength shift of selected dips (dip1 and dip2) in the range of 1450–1570 nm for the case of $L_s \approx 300$ μm. (b) Measured T-sensitivities of 88.04 nm/°C (dip1) and 75.49 nm/°C (dip2), demonstrating the agreements of experimental and theoretical results.

were located in distinct spectral regions—dip1 in the short-wavelength range (1250–1350 nm) and dip2 in the long-wavelength range (1500–1600 nm)—to examine the spectral dependence of temperature sensitivity. In Figs. 9(a) and 10(a), only the spectra corresponding to 25.0, 25.5, and 26.0 °C are presented, as excessive overlap of interference dips at intermediate temperatures
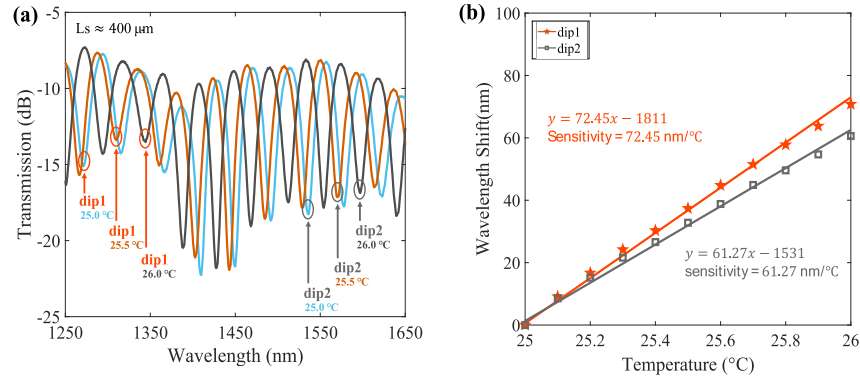
Fig. 10. (a) Evolution of the interference spectra under the same T range for the case of $L_s \approx 400$ µm, showing a comparable dip shift trend. (b) Measured T-sensitivities of 72.45 nm/°C (dip1) and 61.27 nm/°C (dip2), further confirming the reliability of the proposed sensor configuration.

would obscure their identification. The measured temperature sensitivities for the device with $L_s \approx 300$ µm were 88.04 nm/°C for dip1 and 75.49 nm/°C for dip2, as shown in Fig. 9(b). In contrast, Fig. 10(b) shows the device with $L_s \approx 400$ µm exhibited sensitivities of 72.45 nm/°C and 61.27 nm/°C for dip1 and dip2, respectively. These results confirm that interference dips at shorter wavelengths demonstrate higher temperature sensitivity than those at longer wavelengths. This trend is attributed to the spectral dispersion of the liquid-core–cladding mode interference, where the effective refractive index contrast exhibits a steeper spectral slope at longer wavelengths (see Fig. 2(d)). This behavior corresponds to a smaller $\frac{\partial(\Delta n^m_{\text{eff}})}{\partial \lambda}$ at longer wavelengths, thereby resulting in a reduced sensitivity $\frac{d\lambda^m_{dip}}{dT}$, as described in Eq. (8). Additionally, the slightly lower sensitivity observed in the longer L_s configuration is likely due to the altered excitation of higher-order cladding modes (larger m), which exhibit lower temperature sensitivity. These findings suggest strong experimental support for the theoretical model proposed in Eq. (8) and demonstrate excellent agreement with the simulation results in Fig. 5, affirming the accuracy and reliability of the proposed LCFMZI configuration in obtaining precise thermal responses.

4. Conclusion

We have demonstrated a dispersion-engineered liquid-core fiber Mach–Zehnder interferometer (LCFMZI) with ultrahigh temperature (T) sensitivity, potentially exceeding 100 nm/°C. By integrating a Cargille liquid with a high thermo-optic coefficient (TOC) and a low-dispersion refractive index (RI) profile, the proposed sensor exhibits exceptional responsiveness to T variations. The uniquely engineered dispersion structure effectively tailors the OPD, thereby enhancing modal interference and temperature sensitivity. Both theoretical predictions and experimental results show excellent agreement, confirming the reliability and effectiveness of the proposed design. A notable feature of the proposed LCFMZI is its inverse spectral response to temperature changes with $\frac{\partial(\Delta n^m_{\text{eff}})}{\partial \lambda}$ positive, that induces a redshift in the interference spectrum. This phenomenon is attributed to the dispersion engineering of the liquid-core fiber, which ensures that the effective refractive index contrast between the core and cladding modes increases with wavelength. The key parameter governing this behavior is the spectral dispersion of modal index difference. A positive slope of this term leads to redshift under heating, while a negative slope results in blueshift. We further experimentally compared devices with different lengths (Ls) of side-polished HCF$_{75}$ and analyzed dips located in both short and long wavelength regions.

The results revealed that interference dips at shorter wavelengths exhibit higher T-sensitivity. Conversely, dips at longer wavelengths show reduced T-responses that show the inverse spectral response to general fiber-based interferometers. Moreover, the lower sensitivity in the long L_s configuration is observed which is attributed to mode excitation favoring higher-order cladding modes. Lastly, the integration of the HCF_{10} with dual side-polished segments forms an open microchannel, enabling rapid and stable liquid infiltration. The configuration not only supports high-performance sensing but also allows precise optical phase tuning across a broad spectral range. Owing to its compatibility with diverse liquids, high sensitivity, and wide tunability, the proposed LCFMZI represents a promising platform for next-generation high-precision fiber-optic sensing applications.

Disclosures. The authors declare no conflicts of interest.

Data availability. Data underlying the results presented in this paper are not publicly available at this time but may be obtained from the authors upon reasonable request.

References

1. Y. Ma, T. Tian, H. Tan, *et al.*, "A Mach-Zehnder interferometer with two V-shaped cores for refractive index sensing," Sens. Actuators, A **351**, 114189 (2023).
2. Y. Tian, T. Tan, C. Duan, *et al.*, "High sensitivity liquid level sensor based on dual side-hole fiber Mach–Zehnder interferometer," Opt. Commun. **440**, 194–200 (2019).
3. S. Gao, C. Ji, Q. Ning, *et al.*, "High-sensitive Mach-Zehnder interferometric temperature fiber-optic sensor based on core-offset splicing technique," Opt. Fiber Technol. **56**, 102202 (2020).
4. P. Niu, J. Jiang, S. Wang, *et al.*, "Optical fiber laser refractometer based on an open microcavity Mach-Zehnder interferometer with an ultra-low detection limit," Opt. Express **28**(21), 30570–30585 (2020).
5. L. Wang, D. Yi, Y. Geng, *et al.*, "Ultrasensitive deafness gene DNA hybridization detection employing a fiber optic Mach-Zehnder interferometer: Enabled by a black phosphorus nanointerface," Biosens. Bioelectron **222**, 114952 (2023).
6. H. Zhang, M. Zhang, J. Kang, *et al.*, "High sensitivity fiber-optic strain sensor based on modified microfiber-assisted open-cavity Mach-Zehnder interferometer," J. Lightwave Technol. **39**(13), 4556–4563 (2021).
7. Q. Wang, H. Meng, X. Fan, *et al.*, "Optical fiber temperature sensor based on a Mach-Zehnder interferometer with single-mode-thin-core-single-mode fiber structure," Rev. Sci. Instrum. **91**(1), 015006 (2020).
8. W. Zhang, W. Gao, Z. Tong, *et al.*, "Mach–Zehnder interferometer cascaded with FBG for simultaneous measurement of RI and temperature," Opt. Commun. **466**, 125624 (2020).
9. V. Ahsani, F. Ahmed, M. B. Jun, *et al.*, "Tapered fiber-optic Mach-Zehnder interferometer for ultra-high sensitivity measurement of refractive index," Sensors **19**(7), 1652 (2019).
10. Y. Zhang, Y. Wu, Y. Han, *et al.*, "High sensitivity strain sensor based on a novel offset-core single micro-tapered fiber-optic Mach-Zehnder interferometer," Opt. Fiber Technol. **73**, 103012 (2022).
11. H. Z. Ma, Y. Zhang, W. Zhang, *et al.*, "Polymer-coated polishing seven-core Mach-Zehnder interferometer for temperature sensitivity enhancement," Opt. Fiber Technol. **149**, 107774 (2022).
12. H. Zhang, S. Gao, Y. Luo, *et al.*, "Ultrasensitive Mach-Zehnder interferometric temperature sensor based on liquid-filled D-shaped fiber cavity," Sensors **18**(4), 1239 (2018).
13. Z. Zhou, Z. Gong, B. Dong, *et al.*, "Enhanced sensitivity refractometer based on spherical Mach–Zehnder interferometer with side-polished structure," IEEE Sensors J. **21**(2), 1548–1553 (2021).
14. Y. Ma, Y. Yi, X. Li, *et al.*, "Refractometer based on fiber Mach-Zehnder interferometer composed of two micro bending cores," Opt. Express **29**(20), 31443–31454 (2021).
15. S. Liu, H. Zhang, L. Li, *et al.*, "Liquid core fiber interferometer for simultaneous measurement of refractive index and temperature," IEEE Photonics Technol. Lett. **31**(2), 189–192 (2019).
16. A. A. Noman, J. N. Dash, X. Cheng, *et al.*, "Mach-Zehnder interferometer based fiber-optic nitrate sensor," Opt. Express **30**(21), 38966–38974 (2022).
17. D. Xiao, G. Wang, F. Yu, *et al.*, "Optical curvature sensor with high resolution based on in-line fiber Mach-Zehnder interferometer and microwave photonic filter," Opt. Express **30**(4), 5402–5413 (2022).
18. W. Yuan, Q. Zhao, L. Li, *et al.*, "Simultaneous measurement of temperature and curvature using ring-core fiber-based Mach-Zehnder interferometer," Opt. Express **29**(12), 17915–17925 (2021).
19. S. Marrujo-García, I. Hernández-Romano, M. Torres-Cisneros, *et al.*, "Temperature-independent curvature sensor based on in-fiber Mach–Zehnder interferometer using hollow-core fiber," J. Lightwave Technol. **38**(15), 1 (2020).
20. C. Lu, X. Dong, and C. Wu, "Characteristics of critical-wavelength-existed fiber-optic Mach–Zehnder interferometers and their sensing applications," Photonics **9**(6), 378 (2022).

21. C. L. Lee, W. R. Zhuo, and T. K. Liu, "Highly Modulated In-Fiber Mach–Zehnder Interferometer Based on an Ultracompact Leaky-Guided Liquid Core," Sensors **22**(3), 808 (2022).

22. C. L. Lee, J. T. Chao, Y. Z. Huang, *et al.*, "Ultrahigh sensitive liquid-core fiber Mach–Zehnder interferometer using a low light absorption," Opt. Laser Technol. **188**, 112919 (2025).

23. H. Jeong and K. Oh, "Theoretical analysis of cladding-mode waveguide dispersion and its effects on the spectra of long-period fiber grating," J. Lightwave Technol. **21**(8), 1838–1845 (2003).

24. Refractive Index Liquids Available online: (accessed on 4 May 2025) https://cargille.com/wp-content/uploads/2023/01/Refractive-Index-Liquid-Series-A-n-1.4600-at-589.3-nm-and-25%C2%B0C.pdf.

25. K. Okamoto, *Fundamentals of optical waveguides*, (2nd ed.) Academic Press, (2006).

26. https://www.molex.com/en-us/products/capillary-tubing. 987651-3171.pdf Available online: (accessed on 4 May 2025).

27. B. H. Lee, Y. Liu, S. B. Lee, *et al.*, "Displacements of the resonant peaks of a long-period fiber grating induced by a change of ambient refractive index," Opt. Lett. **22**(23), 1769–1771 (1997).

28. C. L. Lee, C. Y. Yeh, and Y. X. Jiang, "Effective liquid-filled leaky-guided fiber Mach–Zehnder interferometer with a side-polished fiber," IEEE Sens. J. **25**(6), 9681–9688 (2025).